Electronic Supplementary Material (ESI) for ChemComm.
This journal is © The Royal Society of Chemistry 2019

Supporting Information

Carbon-free silicon/polyaniline hybrid anodes with 3D conductive structures for superior lithium-ion batteries

Jun Zhou,[a†] Ling Zhou,[a†] Lishan Yang,[*ac] Tao Chen,[b] Jiaqi Li,[a] Hao Pan,[a] Yahui Yang,[a] and Zhongchang Wang[*c]

[a.] *Key Laboratory of Chemical Biology & Traditional Chinese Medicine Research (Ministry of Education of China), National and Local Joint Engineering Laboratory for New Petrochemical Materials and Fine Utilization of Resources, Hunan Normal University, Changsha, Hunan 410081, P.R. China. E- mail: lsyang.chemistry@gmail.com. Tel./Fax.: +86 731-88872531.*

[b.] *School of Chemistry and Chemical Engineering, Central South University, Changsha 410083, China.*

[c.] *Department of Quantum and Energy Materials, International Iberian Nanotechnology Laboratory (INL), Avenida Mestre José Veiga s/n, Braga 4715-330, Portugal.*

† These authors contributed equally to this work.

Experimental section

Fabrication of coral-shaped porous Si dendrites (SD): In a typical synthesis, 2.0 g Al-Si alloy powders (99%, Al:Si = 92:8 Wt.%, Tianjiu Co., Changsha, China) were selectively etched in 300 mL HCl aqueous solution (3 mol L^{-1}) at room temperature for 8 h with stirring. After filtering, the products were washed several times with pure H_2O and ethanol, and dried in vacuum at 60 °C overnight.

Fabrication of SD-PANI hybrid with oxalic acid dopants (SD-OP): Firstly, 100 mg SD was dispersed in 20 mL H_2O solution, which contained 100 mM aniline monomer and 400 mM oxalic acid. The mixture was cooled in an ice bath with sufficient supersonic mixing for 20 minutes. Later, 6.67 mL H_2O solution, which contained 125 mM ammonium persulfate, was added into the above SD mixture and subjected to sonication for 10 minutes. Then, the polymerization process continued for 10 h in a refrigerator (0~5 °C). Finally, the product was filtered and washed thoroughly with distilled H_2O and ethyl ether until the washing solution became transparent, and the SD-OP hybrids were dried in a vacuum oven at 60 °C for 12 h. For other acid doping, a mixture of 1M HCl or 30 mM phytic acid with 100 mM aniline monomer were used.

Battery assembly and characterization

Electrode fabrication: The SD-OP electrode was prepared by spreading the slurry of Si materials, sodium alginate in a weight ratio of 90:10 in deionized water onto copper foils (no additional conductive additive was used) using the doctor-blading technique. Then, the cast films were dried in a vacuum oven at 60 °C for 12 h. For comparison, slurries were prepared by the same procedures, but conductive additive (acetylene black) and binder (sodium alginate) with the weight fraction of 15% and 10% were used in SD electrode, respectively. The mass loading of SD-OP and SD are about 0.3 mg cm^{-1}.

Battery testing: The electrochemical properties of the working electrode were

evaluated with 2032 coin-type cells, with Li foils as the counter electrodes, assembled in an argon-filled glovebox. The electrolyte was prepared by dissolving $LiPF_6$ (1.0 M) into a mixture of dimethyl carbonate and ethylene carbonate (1:1, by volume). An Asahi Kasei microporous polypropylene membrane with a thickness of 25 μm was used as the separator (Asahi Kasei).

Characterization

Powder X-Ray diffraction (XRD) data were recorded with a Rigaku Ultima IV powder diffractometer using Cu-Kα radiation (λ = 1.5405 Å) operated from 20° to 80° (2θ). The morphologies of the samples and EDS mapping images were investigated by field emission scanning electron microscopy (SEM, Verios 460L) and transmission electron microscopy (TEM, Talos F200X) instruments equipped with energy dispersive X-ray spectroscopy. X-ray photoelectron spectroscopy (XPS, ESCALAB 250Xi, Thermo Scientific) was utilized to analyze the surface properties. The FTIR spectra were recorded on a PerkinElmer Frontier Mid-IR FTIR infrared spectroscopy in the range of 1550–800 cm^{-1}. Thermogravimetric analysis was performed on a Netzsch TG 209 F3 device at a heating rate of 10 °C min^{-1} in air. The galvanostatic discharge/charge test of the assembled cells was carried out on a Land battery test system (Land CT2001A) in the potential window of 0.01 to 2.0 V. The current density and the capacity were both calculated on the basis of Si mass. Electrochemical impedance spectroscopy (EIS) was measured over the frequency range of 100 k to 0.01 Hz. Cyclic voltammetry (CV) characterizations were conducted in the potential range of 0.01-2.0 V at a scan rate of 0.1 mV s^{-1}. EIS was conducted on an electrochemical workstation (Princeton Applied Research, USA). Nitrogen absorption isotherms were obtained at 77 K using a Quanta chrome Autosorb-1-C. The surface area of sample and pore size distributions were made by application of the Barrett–Joyner–Halenda (BJH) method to the desorption data.

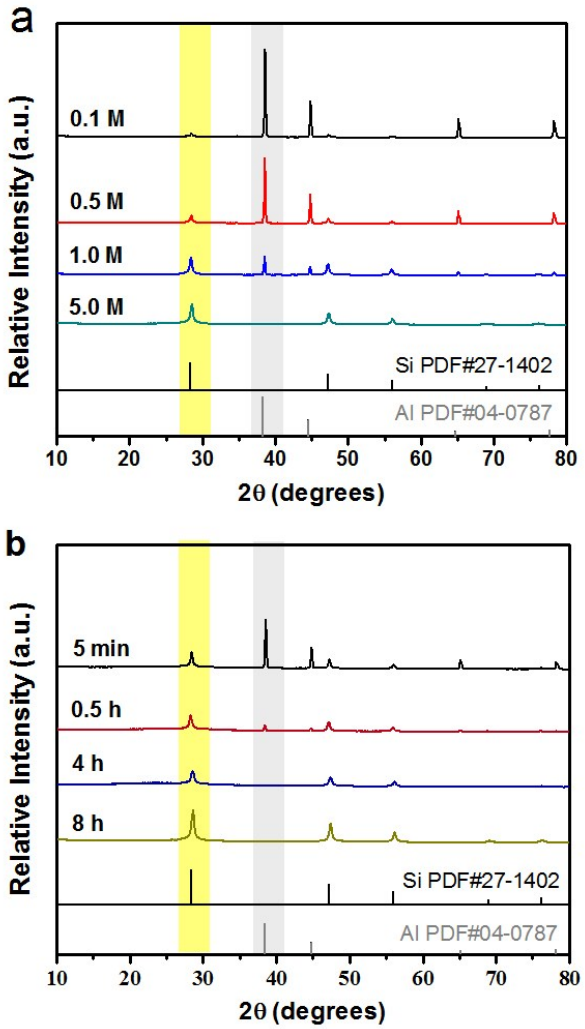

Fig. S1 (a) XRD patterns of $Al_{92}Si_8$ etched in HCl solutions with different concentrations (0.1 M, 0.5 M, 1.0 M and 5.0 M) for 8 h, and (b) in 3.0 M HCl with different etching time (5 min, 0.5 h, 4 h and 8 h).

As shown in Fig. S1a and S1b, the XRD diffraction peaks of the pristine Al-Si alloy powders can be indexed to the co-existence of Al (PDF# 04-0787) and Si (PDF# 27-1402) metals. Along with the increasing acid concentration and etching time, the Al peaks within the Al-Si alloys are gradually removed by leaving the pure Si phase. Diffraction peaks of Si located at 2θ = 28.4°, 47.2°, 56.1°, 69.1° and 76.3°, are related to the (111), (220), (311), (400) and (331) crystal planes of Si.

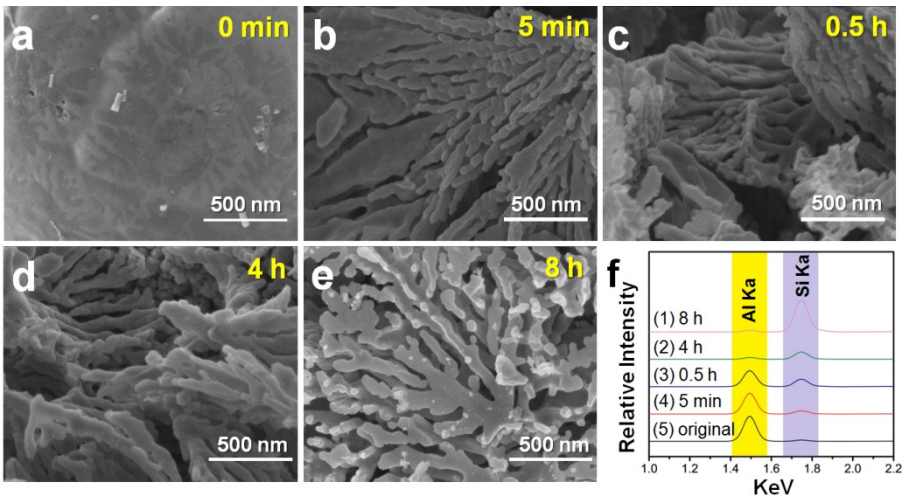

Fig. S2 (a-e) SEM images of the Al-Si alloy samples during the de-alloying process: 0 min, 5 min, 0.5 h, 4 h and 8 h. (h) Corresponding XRF results showing the Al/Si content evolution during the de-alloying process.

After immersion of the Al-Si alloy powders in 3M hydrochloric acid for 5 minutes, coral-like structures appeared and transformed totally with longer etching time (Fig. S2). The overall-size of a SD particle is ~10 μm (Fig. 1c), and its porous coral-shaped ligament are approximately 10-100 nm. After reaction for 4 hours (SD-4), the structure of coral-shaped nano-channels were basically formed, which is similar to those etching for 8 hours (SD-8). With longer etching time, slight amount of Al could not be thoroughly removed. In this work, Si dendrites obtained with 8 h etching in 3 M HCl were chosen as the intermediate SD product for the following PANI coating experiments.

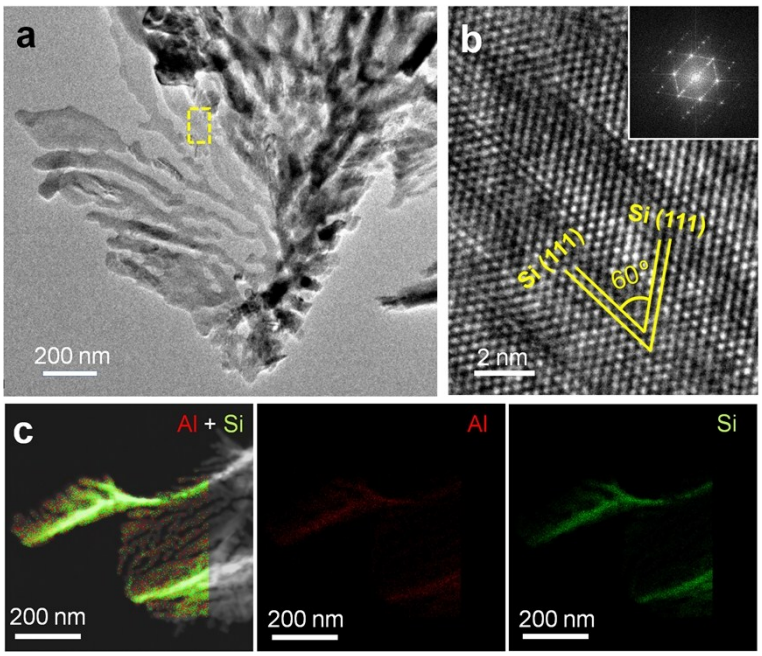

Fig. S3 (a) A TEM image of a SD dendrite. (b) The magnified HRTEM image of the selected frame in (a). (c) Mapping results of a SD dendrite from the SD-8h sample.

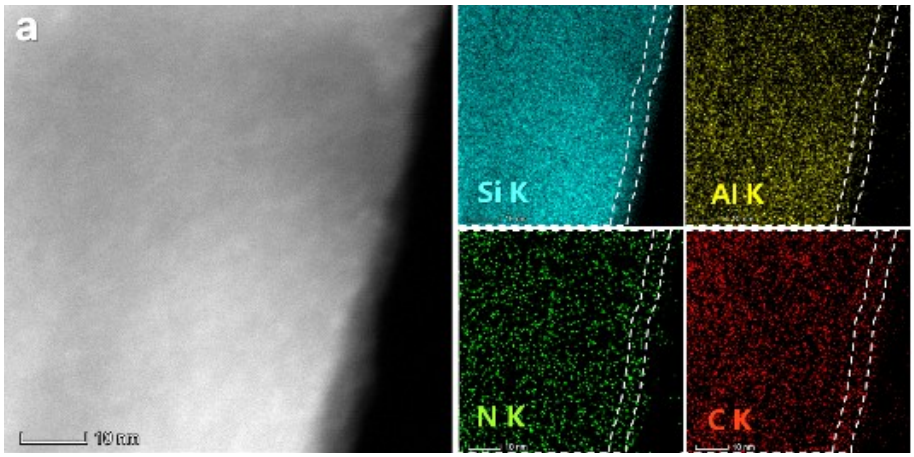

Fig. S4 (a) A STEM image of the edge part from a SD-OP dendrite, and (b) the corresponding EDS elemental mapping images of Si, Al, N, and C.

From the EDS elemental mapping images, elements N/C are found to distribute closely around Si and slightly exceed the SD-OP ligament outline (in white). However, the distribution of element Al is within the dashed box and smaller than the distribution of Si. Combined with the HRTEM and XPS results (Fig. 1g, 2c and 2d), the PANI/SiO_x/Si ternary hybrid structure of the SD-OP anode could be finally revealed.

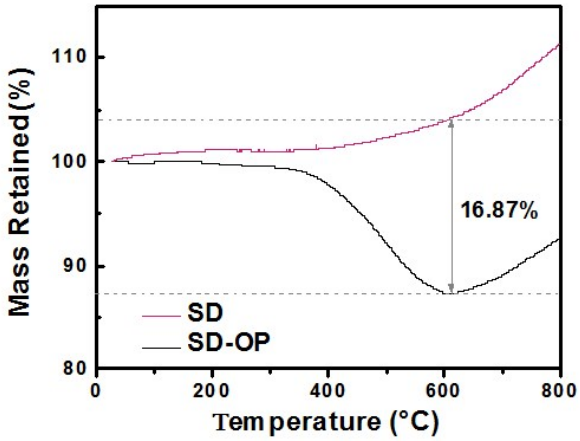

Fig. S5 Thermogravimetric analysis (TGA) curves of SD and SD-OP samples in air.

As shown in **Fig. S5**, the weight of the prepared SD increases above 500 °C is due to the oxidation of silicon. For SD-OP hybrid sample, the weight decreases since 400 °C and the increase above 600 °C might be related to the oxidations of carbon and silicon in air, respectively.[1]

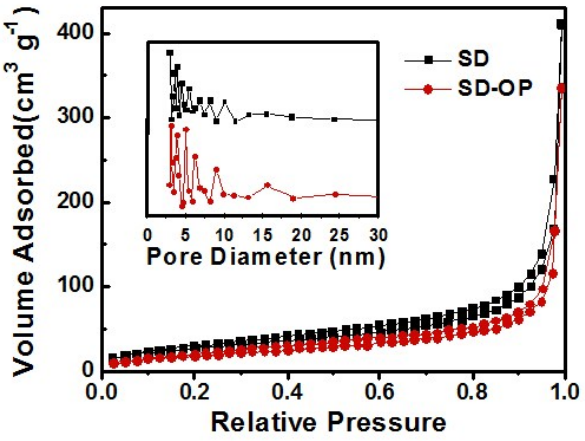

Fig. S6 Nitrogen adsorption and desorption isotherms, (Inset) Pore size distribution of the porous Si and Si/PANI composites.

The Brunauer-Emmett-Teller (BET) method have been applied to evaluate the specific surface areas of SD (100.74 m^2 g^{-1}) and SD-OP (70.028 m^2 g^{-1}) samples, therefore confirming the pore generation by chemical etching and PANI coating for the Si dendrites.

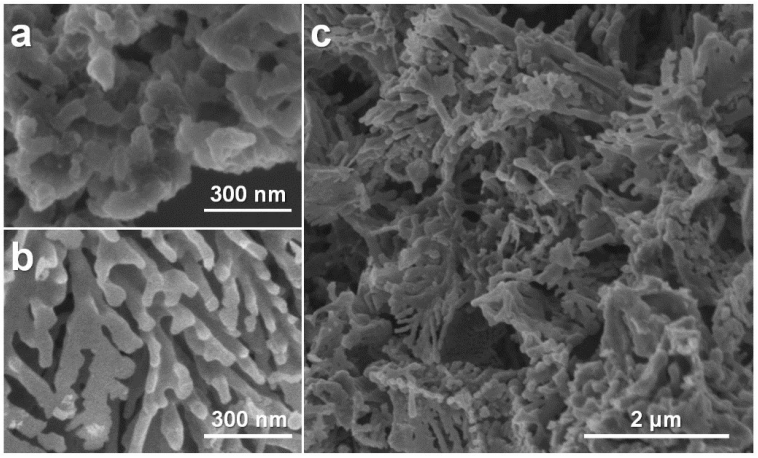

Fig. S7 SEM images of (a) oxalic acid doped polyaniline (OP), (b) pure coral-shaped SD, and (c) SD-OP hybrids.

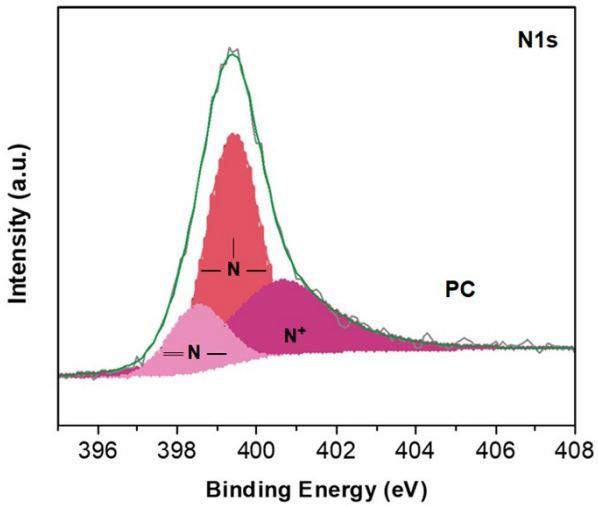

Fig. S8 XPS spectra of the N element in oxalic acid doped polyaniline.

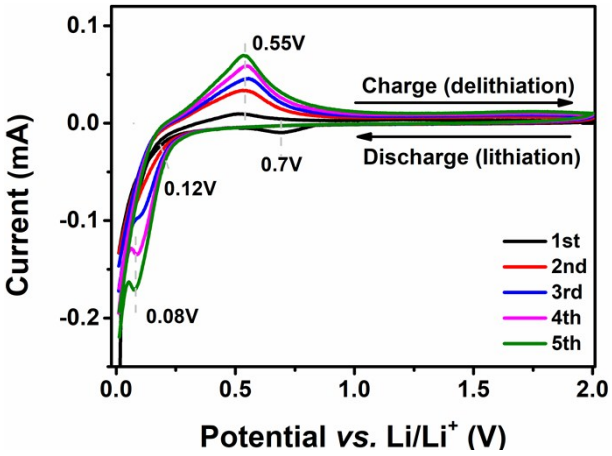

Fig. S9 CV curves in the initial five cycles of the SD-OP anode.

Fig. S9 discloses the cyclic voltammetry (CV) curves of SD-OP acquired at a scan rate of 0.1 mV s^{-1} over the potential window of 0.01-2.00 V. In the first cathodic scan, there are two small peaks at 0.12 V and 0.7 V, which could be attributed to the formation of a thin solid electrolyte interphase (SEI) layer at the electrode/electrolyte interface.[2] A sharp redox peak at 0.08 V corresponds to the formation of the Li_xSi phase and the peaks at 0.55 V is ascribed to the delithiation process from the amorphous Li_xSi to Si.[3] The magnitude of the current peaks increased with cycling due to activation of more material to react with Li in each scan.[4]

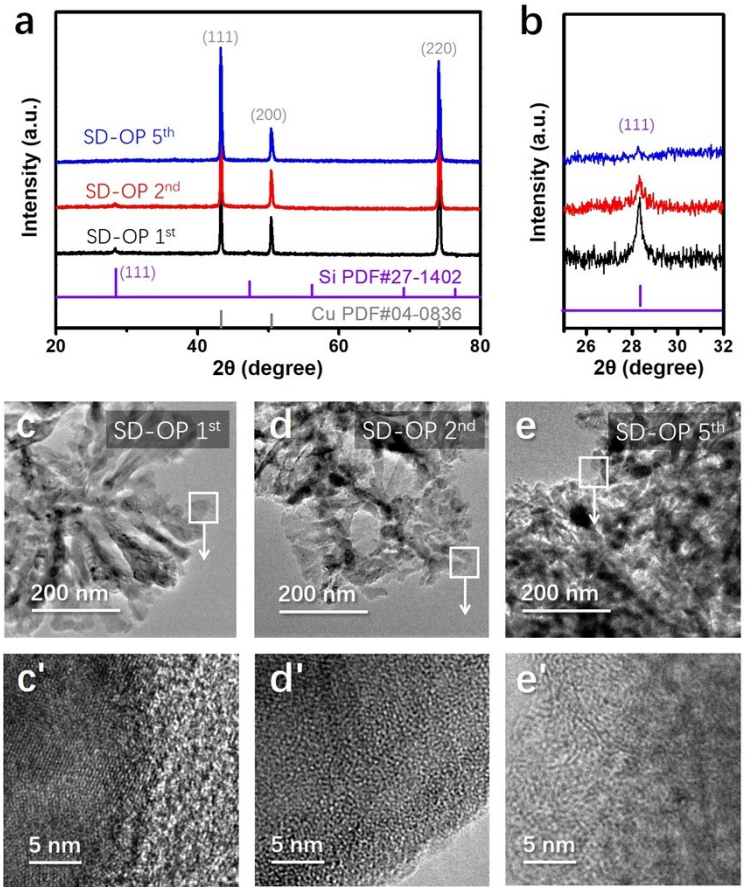

Fig. S10 (a) Ex-situ XRD curves of SD-OP anodes after the 1st, 2nd and 5th cycles. (b) Enlargement of the XRD pattern in the 2*θ* range of 25−32°. Ex-situ TEM and corresponding HRTEM images of cycled SD-OP materials after the 1st cycle (c, c'), the 2nd cycle (d, d'), and the 5th cycle (e, e').

Fig. S10a displays the XRD patterns of three SD-OP anodes, which can be indexed as the copper foil (PDF#04-0836) and silicon (PDF#27-1402). Obviously, the Si (111) peak strength weakens from the 1st cycle to the 5th cycle, indicative of structure degradation of the silicon as a result of the lattice expansion and contraction during the electrode process.[7,11] Moreover, such a structure variation can also be clearly revealed by the TEM and HRTEM images of the silicon materials from corresponding anodes with various cycles, in which the dense silicon crystalline structure in **Fig. S10c´** gradually turns into the loose amorphous structure in **Fig. S10e´**.

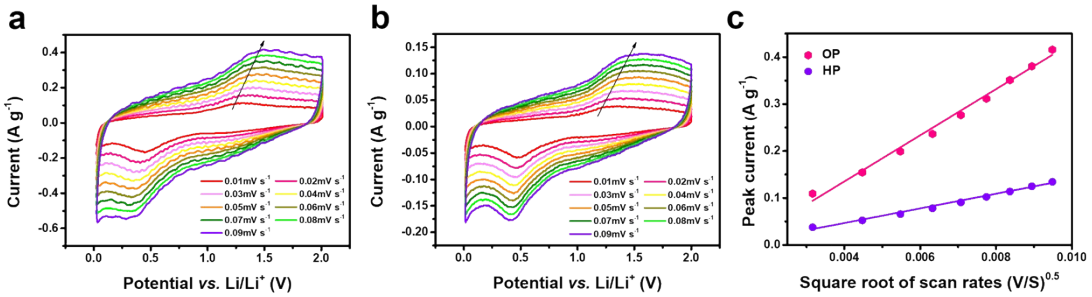

Fig. S11 CV profiles of two kinds of PANI electrodes with varying sweeping rates: (a) oxalic acid doped PANI (OP) and (b) HCl doped PANI (HP). (c) Linear fits for the anodic peak current versus square root of scan rate of electrodes with different acid doped PANI.

The Li-ion diffusion coefficient was evaluated according to the Randles-Sevick equation:[5-7]

$$Ip = (2.69 \times 10^5)\, n^{1.5}\, S\, D_{Li+}^{0.5}\, C_{Li}\, \nu^{0.5}$$

Where Ip is the peak current, n is the charge-transfer number, S is the contact area between electrolyte and electrode, D is the diffusion coefficient of Li-ion, C is the Li-ion concentration in the electrolyte, and ν is the scanning rate. The slope of the curve ($Ip/\nu^{0.5}$) represents the lithium ion diffusion rate (as n, S, and C_{Li} are unchanged). The slopes of curves in **Fig.S11** are positively correlated to the corresponding lithium ion diffusion, which indicates that the PANI doped with HCl has a lower diffusivity than the oxalic acid doped PANI.

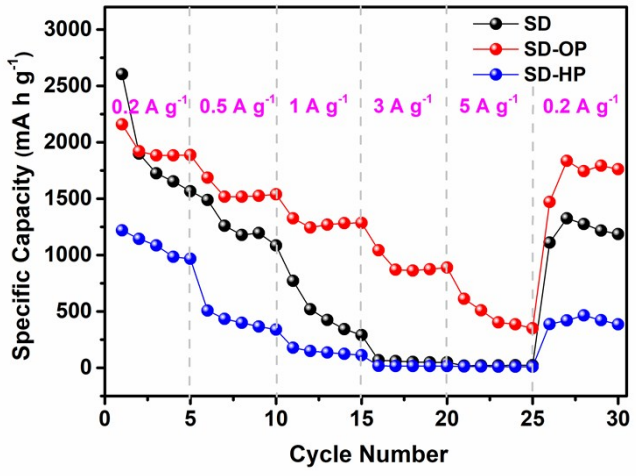

Fig. S12 Rate capability of SD, SD-HP and SD-OP anodes.

The rate performance of SD and SD-OP is shown in **Fig. S12**, the specific capacity of SD-OP tested at different densities is much enhanced by comparing with that of the non PANI combined SD anode, especially at high charging rates. Interestingly, compared with SD-OP hybrid anode, SD-HP anode exhibits poor Rate capabilities which even worse than SD, which is consistent with cycling performance in **Fig. S16**.

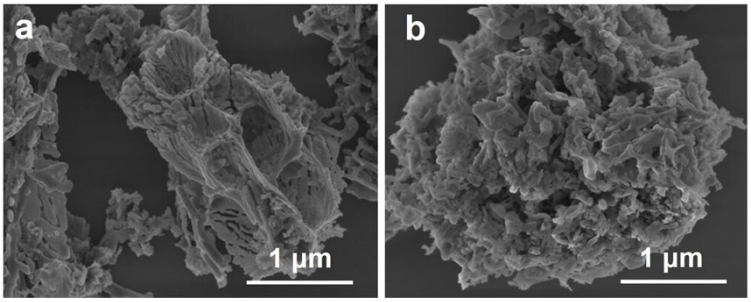

Fig. S13 SEM images of hybrid anodes fabricated with different acids: (a) oxalic acid doped PANI (SD-OP), and (b) HCl doped PANI (SD-HP).

From the results of **Fig. S11**, oxalic acid-doped polyaniline shows better ion conductivity than the polyaniline sample doped with HCl. Due to the weak bonding effect of the polymer on Si (**Fig. S13**), the self-agglomeration is quite obvious in the HCl doped silicon/polyaniline hybrid anode. Since substantial Polyaniline coating may hinders the transport of lithium ions and causes capacity decay, the thickness of Polyaniline coating in electrode material is usually less than 10nm.[8-10] As for SD-OP, the interactions between -OH groups and the carboxyl result in the evenly coating of oxalic acid molecules on the surface of SD, which may further crosslink with aniline monomers during polymerization to generate a conformal conductive coating, that is similar to phytic acid doped conducting hydrogel.[11]

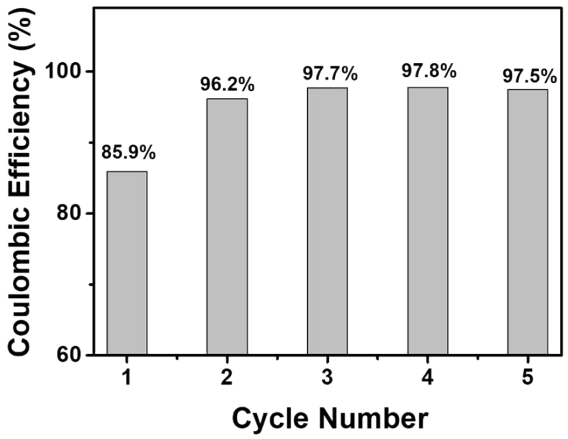

Fig. S14 Coulombic efficiency of the SD-OP anode at the initial five cycles under a current density of 0.2 A g^{-1}.

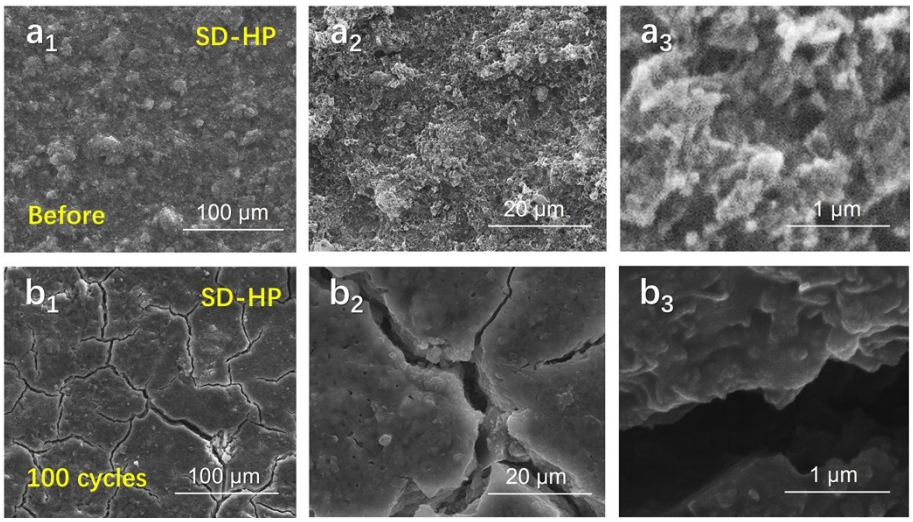

Fig. S15 SEM images of the SD-HP electrode pads: (a_1-a_3) before cycling, and (b_1-b_3) after 100 cycles (at different magnifications: 100 μm, 20 μm and 1 μm).

In order to compare the electrochemical stabilities of SD-OP and SD-HP cathodes, we also studied the SEM images of the SD-HP electrode pads before and after cycling (**Fig. S15**). Unlike the compact surface of SD-HP samples before cycling, clear cracks would be observed after 100 cycles. What's more, the cracks are more obvious in the SD-HP electrode pad after 100 cycles than that of the raw silicon dendrite even after 500 cycles. Significant structural degradation of SD-HP electrode would lead to a rapid decay of its capacity, which is consistent with the corresponding cycling performance.

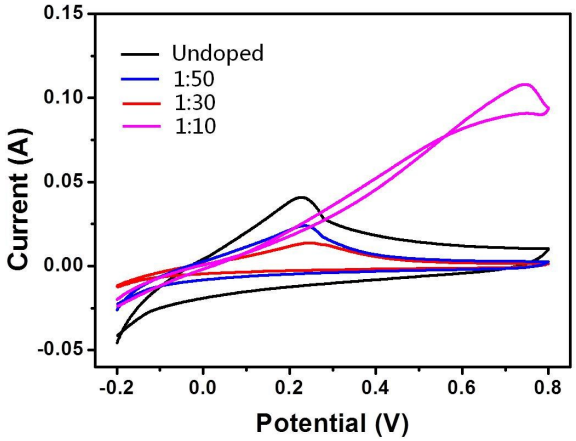

Fig. S16 CV curves of four PANI electrodes without Al^{3+} (undoped sample) and with three different Al^{3+} doping ratios (Al^{3+}: An = 1:50, 1:30, and 1:10).

In order to verify the effect of Al^{3+} on PANI, we separately synthesized PANI containing different Al^{3+} doping amounts (undoped, Al^{3+}: An = 1:50, 1:30, and 1:10), and studied the CV results of these samples (**Fig. S16**). The movement of the oxidation peak and the significant reduction in the integrated area show that the electrochemical activity of PANI is very sensitive to the Al^{3+} dopant. Theoretically, Al^{3+} can induce the inter-chain cross-linking of PANI and inhibit the peristaltic and electrical conductivity of the PANI chains. In this work, the exact mechanism still needs further research.

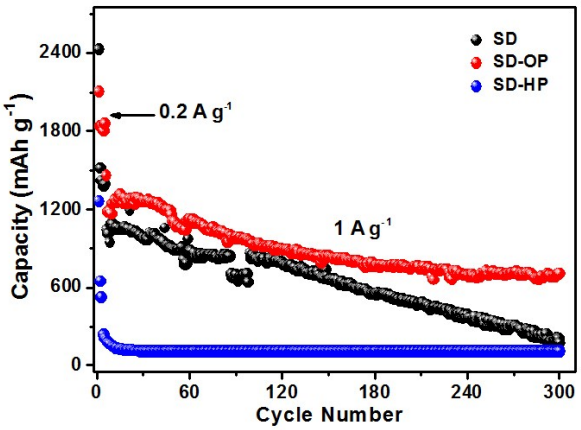

Fig. S17 Cycling performance of the SD, SD-OP and SD-HP anodes in half-cells.

It is clear that the SD-OP anode shows a higher capacity and better stability than the pure silicon dendrites (SD) anode (**Fig. S17**). However, the SD-HP anode totally cannot support a stable charge/discharge at such a high rate. As we discussed earlier, the use of HCl might yield the production of a small amount of Al^{3+} dissolved form silicon dendrites during the PANI polymerization, which would finally cause the uncontrollable cross-linking and the poor conductivity of the PANI.

Table S1 XRF results of $Al_{92}Si_8$ alloy that etched in 3 M HCl for 0 min, 5 min, 0.5 h, 4 and 8 h, respectively.

Samples	Wt.%		Atom. %	
	Si	Al	Si	Al
$Al_{92}Si_8$ alloy	7.408	92.592	7.138	92.862
5 min etching	17.467	82.533	16.897	83.103
0.5 h etching	34.821	65.179	33.917	66.083
4 h etching	74.940	25.060	74.180	25.820
8 h etching	92.044	7.956	91.745	8.2545

Table S2 Infrared peaks of the SD-OP and polyaniline (OP) samples.

Bonding type	OP (cm^{-1})	SD-OP (cm^{-1})
Quinoid ring –C=C– stretching vibration	1584	1590
Benzene ring –C=C– stretching vibration	1497	1501
Aromatic secondary amine C–N stretching vibration	1301	1307
Quinone ring N=(C_6H_4) =N stretching vibration	1138	1147
Vibration absorption of out-of-plane bending vibration of benzene ring C–H	804	833

Compared to pure OP materials, some of the FTIR absorptions for the SD-OP hybrid shifted to shorter wavenumbers, whereas other bands shifted to longer wavenumbers. These FTIR results indicated that a series of electrostatic forces and hydrogen bonding interactions existed in oxalic acid doped Si/PANI hybrids.[12]

Table S3 Equivalent circuit parameters obtained from corresponding EIS spectra of the same SD-OP anode with different cycle numbers.

Sample	R_s (Ω)	R_{ct} (Ω)
SD-OP 1st	3.95	950.2
SD-OP 3rd	3.41	313.4
SD-OP 100th	3.64	352.2

In **Table S3**, all the equivalent circuit parameters of the SD-OP anode were obtained after charge/discharge operations between 0.01−2.0 V at 1 A g^{-1} with different cycles. The equivalent circuit, R_s represents electrolyte and electrode resistance, R_{ct} is the charge transfer resistance, CPE is the double-layer capacitance and W_s reflects the Warburg impedance.[8] Apparently, the R_{ct} value and the Warburg diffusion coefficient of the SD-OP electrode after 1 cycle are the largest among three samples; after 3 cycles, the R_{ct} of the SD-OP electrode decrease, which may be due to the slow wetting electrolyte into porous electrodes and the increased electrical conductivity of the silicon during the charge-discharge processes, and then, the structure of the SD-OP electrode gradually becomes stable.[11] Interesting, when the cycle number increases to 100, the R_s and R_{ct} values of the SD-OP electrode grow slightly, which may be ascribed to the stable structure and SEI of the silicon,[12] and the charge transfer resistance and the Warburg diffusion coefficient of DS-OP at the 100th cycle are larger than those of the 3rd cycle, which may be ascribed to the more obvious volume change of the silicon.[13]

References

1 R. T. Xu, G. Wang, T. F. Zhou, Q. Zhang, H. P. Cong, S. Xin, J. Rao, C. F. Zhang, Y. K. Liu, Z. P. Guo and S. H. Yu, *Nano Energy*, 2017, **39**, 253–261.

2 Q. Z. Chen, R. L. Zhu, Q. Z. He, S. H. Liu, D. C. Wu, H. Y. Fu, J. Du, J. X. Zhu and H. P. He, *Chem. Commun.*, 2019, **55**, 2644–2647.

3 W. He, Y.J. Liang, H. J. Tian, S. L. Zhang, Z. Meng and W. Q. Han, *Energy Storage Mater.*, 2017, **8**, 119-126.

4 C. K. Chan, H. L. Peng, G. Liu, K. McIlwrath, X. F. Zhang, R. A. Huggins and Y. Cui, *Nat. Nanotechnol.*, 2008, **3**, 31.

5 G. Zhou, H. Tian, Y. Jin, X. Tao, B. Liu, R. Zhang, Z. W. Seh, D. Zhuo, Y. Liu, J. Sun, J. Zhao, C. Zu, D. S. Wu, Q. Zhang and Y. Cui, Proc. *Natl. Acad. Sci. U. S. A.*, 2017, **114**, 840.

6 R. N. Guo, S. L. Zhang, H. J. Ying, W. T. Yang, J. L. Wang and W. Q. Han, *ChemSusChem*, 2019, **12**, 4838–4845.

7 X. Y. Tao, J. G. Wang, C. Liu, H. T. Wang, H. B. Yao, G. Y. Zheng, Z. W. Seh, Q. X. Cai, W. Y. Li, G. M. Zhou, C. X. Zu and Y. Cui, *Nat. Commun.*, 2016, **7**, 11203.

8 Y. N. Luo, R. S. Guo, T. T. Li, F. Y. Li, Z. C. Liu, M. Zheng, B.Y. Wang, Z. W. Yang, H. L. Luo and Y. Z. Wan, *ChemSusChem*, 2019, **12**, 1591–1611.

9 H.W. Mi, X. D. Yang, F. Li, X. Q. Zhuang, C. X. Chen, Y. L. Li and P. X. Zhang, *J. Power Sources*, 2019, **412**, 749–758.

10 X. M. Zhou, Y. Liu, C. Y. Du, Y. Ren, T. S. Mu, P. J. Zuo, G. P. Yin, Y. L. Ma, X. Q. Cheng and Y. Z. Gao, *J. Power Sources*, 2018, **381**, 156–163.

11 H. Wu, G. H. Yu, L. J. Pan, N. Liu, M. T. McDowell, Z. N. Bao and Y. Cui, *Nat. Commun.*, 2013, **4**, 1943.

12 P. P. Kong, H. X. Feng, N. L. Chen, Y. Lu, S. Y. Li and P. Wang, *Chem. Commun.*, 2019, **9**, 9211–9217.

13 S. T. Guo, H. Li, Y. Q. Li, Y. Han, K. B. Chen, G. Z. Xu, Y. J. Zhu and X. L. Hu, *Adv. Energy Mater.*, 2018, **8**, 1800434.